

Article

Simplified Damage Assessment Tool for Rails and Crossings Based on Standard Wear and RCF Models

Georg Schnalzger ¹, Werner Daves ¹, Jürgen Maierhofer ^{1,*}, Uwe Ossberger ², Heinz Ossberger ², Christian Bucher ² and Martin Pletz ³

¹ Materials Center Leoben Forschung GmbH, A-8700 Leoben, Austria

² Voestalpine Railway Systems GmbH, A-8740 Zeltweg, Austria

³ Department of Polymer Engineering and Science, Montanuniversität Leoben, A-8700 Leoben, Austria

* Correspondence: juergen.maierhofer@mcl.at; Tel.: +43-3842-459-2241

Abstract: A numerical tool is proposed to simultaneously assess various damage mechanisms that are driven by contact loading. The tool transfers loads to the contact-patch level using three contact parameters: the maximum contact pressure (p_{\max}), the creepage (c) and the contact length ($2a$). The local wear and RCF predictions are implemented based on existing models from the literature. The load input can originate from numerical vehicle–track simulations or manual input of the user. The assessment tool is applied for a finite element analysis of a fixed manganese crossing nose to prove its validity. The algorithm is implemented via an automated Python code, which, on the one hand enables damage prediction for track components based on standard damage models. On the other hand, knowledge of novel local contact damage models can be transferred to the scale of track components.

Keywords: wheel–rail contact; wear; rolling contact fatigue; finite element method; switches and crossings; rails



Citation: Schnalzger, G.; Daves, W.; Maierhofer, J.; Ossberger, U.; Ossberger, H.; Bucher, C.; Pletz, M. Simplified Damage Assessment Tool for Rails and Crossings Based on Standard Wear and RCF Models. *Metals* **2022**, *12*, 2169. <https://doi.org/10.3390/met12122169>

Academic Editor: Yizhu He

Received: 3 November 2022

Accepted: 12 December 2022

Published: 16 December 2022

Publisher's Note: MDPI stays neutral with regard to jurisdictional claims in published maps and institutional affiliations.



Copyright: © 2022 by the authors. Licensee MDPI, Basel, Switzerland. This article is an open access article distributed under the terms and conditions of the Creative Commons Attribution (CC BY) license (<https://creativecommons.org/licenses/by/4.0/>).

1. Introduction

Railway switches and crossings (S&C) are key components of railway infrastructure, as they guide trains between tracks. Discontinuities in the rail geometry of fixed crossings lead to exceptionally high dynamic loads and creepage at the crossing nose [1]. Consequently, enhanced failure rates are observed compared to regular tracks. As a result, turnout maintenance and replacement account for a significant proportion of operational costs [2]. The repeated rolling–sliding contact between wheels and rail drives two distinctive damage mechanisms: wear and rolling contact fatigue (RCF). Plastic deformation in the rail additionally influences both failure modes due to geometrical adaptations affecting the contact conditions [3]. In the literature, five different main categories of wear are distinguished, namely oxidative wear (or corrosion wear), adhesive wear, abrasive wear, delamination wear and thermal wear [4]. RCF is subdivided into surface and subsurface RCF, depending on the initiation location of cracks [5,6]. The propagation of RCF cracks may cause fatigue fracture, leading to rail breakage [4]. Figure 1 displays typical damage patterns observed in S&C components.

In the past, extensive effort has been put into predictive damage assessment of S&C components. Dynamics as the wheel passes the crossing have been studied with numerical models to quantify contact forces, stresses and geometries. Finite element analysis (FEA) [1,3,7–11] and multibody simulation (MBS) [12] represent the most common applied numerical simulation methods. A couple of approaches combine FEA and MBS, for example, Refs. [2,13]. Several numerical models use rail geometries measured in the field to account for run-in conditions [7,14]. Secondly, predictive wear and RCF models have been developed to predict degradation in railway systems. Wear predictions are based either on Archard's wear law [15] or the so-called T-gamma model [16]. However, both

approaches require extensive calibration of wear coefficients [17]. Nevertheless, Archard's model has been successfully applied to predict wear loss in S&C components [2,13]. To estimate the risk of surface crack initiation, Ekberg et al. [5] proposed a predictive RCF model based on the shakedown theory. The model was applied to railway wheels [5] and, recently, also to the crossing nose using dynamic FEA [18]. Daves et al. [19] presented a numerical model to estimate the growth of surface-initiated cracks considering plasticity and realistic rolling–sliding contact conditions.



Figure 1. Degradation of railway crossing noses: (a) plastic deformation and wear of a manganese crossing nose and (b) material breakouts and spalling/pitting at the crossing nose surface.

Dang Van (DV) [20] introduced a multiaxial damage criterion to predict high cycle fatigue (HCF) in ball bearings. The DV criterion has also been applied to railway components [5,11]. Ekberg et al. [5] proposed a simplified DV criterion and evaluated subsurface damage in railway wheels. Finally, several multicriteria prediction models simultaneously considering various damage modes were proposed in the literature. In [5,21,22], for example, tailored models for railway wheels were presented. Approaches for damage prediction in the track system [23,24], the switch rail [2,25,26] and the crossing nose [18] have also been proposed.

However, the existing prediction models are generally embedded into tailored calculation routines requiring specific simulation or test techniques. In the present work, we attempt to transfer the results of known wear and RCF models from the literature to in-field application. A numerical tool is presented to transfer contact loads from vehicle–track dynamics and assess the wear and RCF degradation using the maximum contact pressure (p_{max}), the creepage (c) and the contact length ($2a$). Comparable local damage assessment approaches were recently proposed by Daves et al. [19] and Zani et al. [27] to assess the growth of RCF cracks in rails and investigate RCF problems in railway components, respectively.

The contact load parameters required for the new assessment tool originate either from vehicle–track dynamics or manual user input. A range of simulation methods such as FEA or MBS, as well as user-defined test data, is feasible. Archard's wear law and two RCF models (surface fatigue index model and DV criterion) from the literature are implemented. In the future, the algorithm can also use more advanced local damage models such as the crack models proposed in [19,28,29].

The tool plots critical damage regions for different failure mechanisms in damage maps and shows at which instances the vehicle–track models fall into those regimes. A case study demonstrates the application of the tool in combination with an FE simulation. A manganese steel crossing nose, which is monitored intensively in the track, is assessed.

The load transfer is verified using literature results and validated with experimental track data. The tool is intended for use by railway operators, as well as rail and crossing manufactures.

The novelty of the work comprises the implementation of damage models for rails based on different available wheel–rail interaction simulations. Additionally, the visualization of all damage variables within two diagrams (i.e., wear and RCF map) allow for evaluation of interactions between different damage mechanisms.

2. Materials and Methods

This section first presents the basic ideas and development of the simplified damage assessment framework. The implementation of standard wear and RCF models is explained step by step. Second, the case study performed to demonstrate the application of the new damage prediction approach is introduced. This includes a detailed description of the finite element analysis (FEA) and field tests.

2.1. Simplified Damage Assessment Tool

The numerical framework aims at predicting wear and RCF on the local contact-patch level to bridge the gap between global vehicle–track interactions (VTI) and local damage processes. The input comprises three contact load variables (p_{\max} , c and $2a$), system variables (train speed, material and friction coefficient) and information about the traffic situation (tonnage and distribution of wheel types). The latter input defines the distribution of different wheel profiles among the total traffic considered for the damage accumulation. For now, standard wear and RCF models from the literature are adapted. By combining them with standard contact models, they are implemented into the algorithm and visualized in two types of damage maps: the wear and RCF maps. The wear and RCF maps show the material-dependent damage regimes and their dependence on the local contact variables. For the prediction of damage of a specific track component, the local contact loads (i.e., p_{\max} , c and $2a$) on the surface of the component are determined for different wheel types using numerical models and plotted in the damage maps as working points. For each working point, the corresponding damage indicators (DIs) are extracted from the damage maps and accumulated for the investigated traffic situation using information on the tonnage. Finally, the accumulated damage is plotted along the investigated component in the assessment diagram to highlight critical damage regions, as shown schematically in Figure 2.

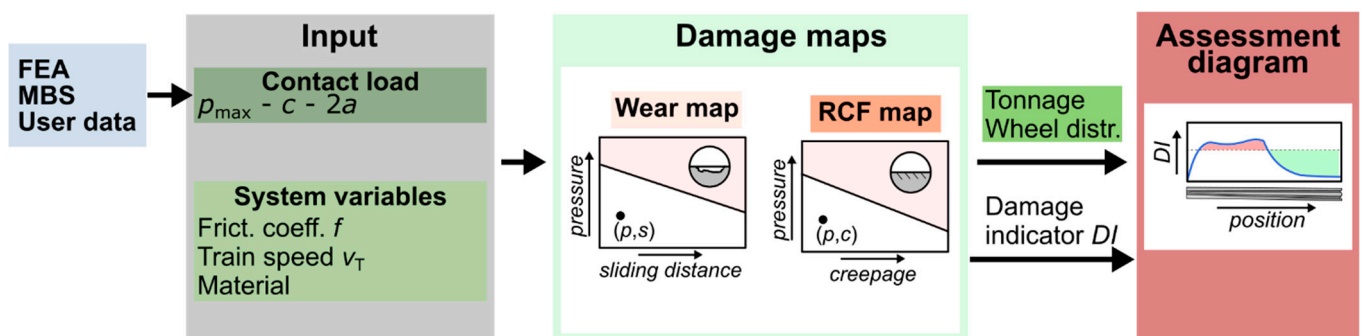


Figure 2. Calculation procedure of the simplified damage assessment tool to assess wear and RCF with standard models on the local contact-patch level based on load data from FEA, MBS or manual input by the user and loading statistics (tonnage and wheel distribution).

The contact load variables capture the load on the contact-patch level for a single load case or traffic condition characterized by the axle load, as well as the wheel and rail geometries. For an elliptical contact patch, p_{\max} and $2a$ are obtained from a two-dimensional cut along the local slip direction, as shown in Figure 3.

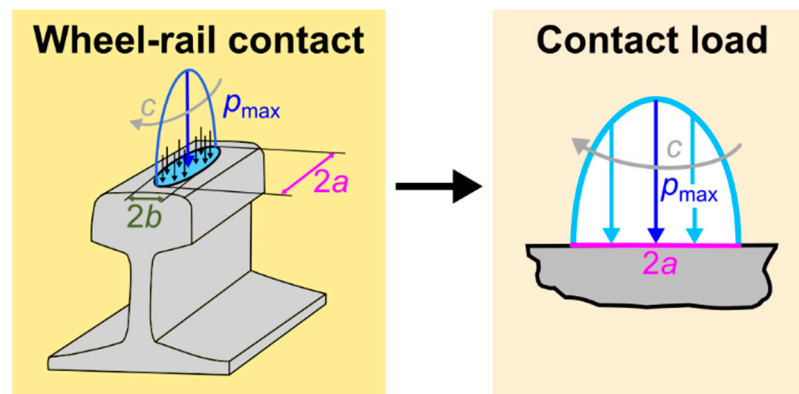


Figure 3. Definition of p_{max} , c and $2a$ for an elliptical contact patch with width $2b$. Note: the contact pressure distribution shown in the figure is schematic and refers to a quasistatic load case. The computations consider the development of slip during contact.

The global creepage (c), which correlates with the local slip in the contact patch, is calculated as:

$$c = \frac{v_T - \omega \times R}{v_T}, \tag{1}$$

where v_T is the train speed, ω is the angular wheel velocity and R is the corresponding rolling radius.

The tonnage and wheel distribution define the distribution of different single-load cases among the total traffic scenarios. This input is either derived from field observations or is specified by the user. The system variables coincide either with data from vehicle–track simulations and field tests or the user defines them. The failure models are implemented into the standardized calculation scheme shown in Figure 4 and plotted in damage maps. The scheme relies on damage functions depending exclusively on the previously defined input parameters. For implemented damage functions, the corresponding damage index can be determined efficiently in a single step for a given contact load. In the following section, the integration of standard wear and RCF models from the literature is outlined in detail.

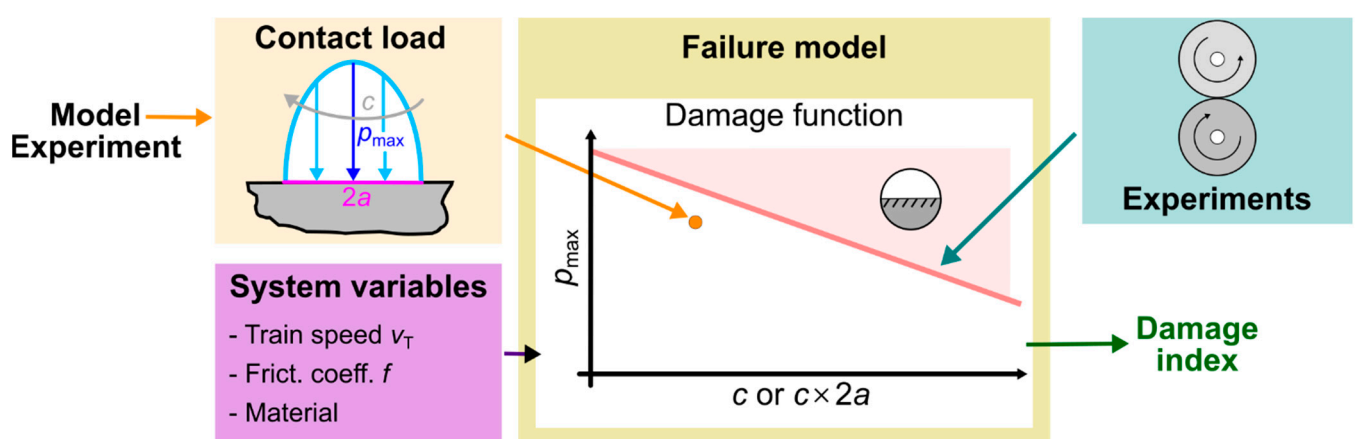


Figure 4. Standardized calculation scheme to implement failure models and efficiently compute damage indices at the local contact-patch level.

2.1.1. Wear Map

The present wear model builds on the Archard wear equation [15]. As proposed in [30], wear is computed on the local contact-patch level using p_{\max} , c and $2a$. The wear depth (Δz) is calculated for a longitudinal cut through the contact patch (Figure 3) as:

$$\Delta z = p_m \times (2a \times c) \times \frac{K}{H}, \quad (2)$$

where p_m is the average contact pressure in the longitudinal direction. The present work assumes a semi-ellipsoidal Hertzian pressure distribution, hence p_m is defined in as $(2/3)p_{\max}$ [31]. The product of $2a$ and c equals the sliding distance, presuming a constant sliding velocity throughout the contact patch. H is the material hardness, and K is the dimensionless wear coefficient. For now, K is taken from [30,32]. In the future, wear charts from twin-disc testing will be calibrated. The wear chart defines K as function of the contact pressure (p) and the sliding velocity (v_{slip}), which is calculated as the product of the train speed (v_T) and creepage (c):

$$v_{\text{slip}} = v_T \times c \quad (3)$$

The results of the wear model are illustrated as a function of the maximum contact pressure normalized by the material hardness and the creepage in a wear map. Figure 5 presents an exemplarily wear map. The presumed wear coefficients (K) amount to 2.9×10^{-4} , 3.5×10^{-3} and 3.5×10^{-2} for the mild, severe and seizure wear regime, respectively. The assumed train velocity amounts to 90 km/h [30].

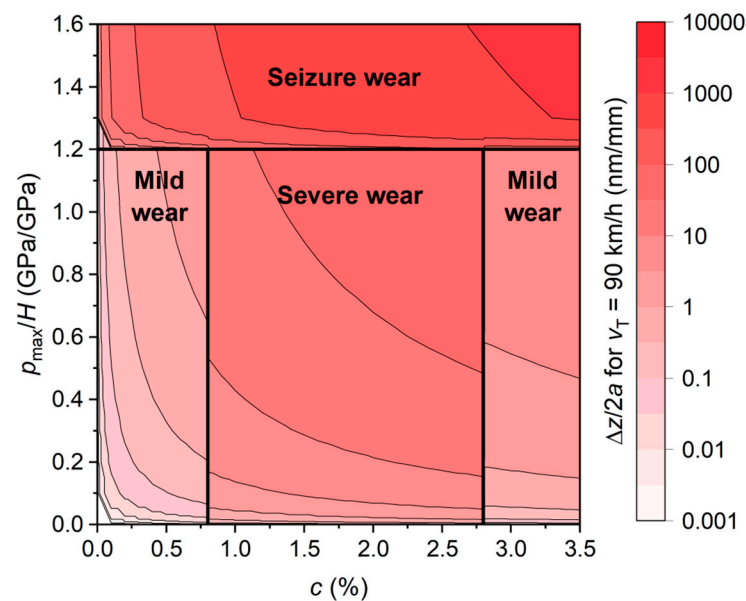


Figure 5. Wear map showing the wear depth per contact length computed using the adapted Archard wear model. The presumed constants are stated in the main text.

The wear area (A_w) produced by the contact patch in a cross section (see Figure 6) is calculated under the assumption of an elliptic sliding distance distribution in the lateral direction (y -axis) from the wear depth (Δz) as [33]:

$$A_w = 0.78 \times \Delta z \times 2b, \quad (4)$$

where b is the lateral contact patch width, which can be estimated from vehicle–track simulations. A_w can also be calculated from rail profiles measured in the field. Hence, it is an important quantity to validate predictions with field measurements. For multiple-load cases, the lateral positions can vary, which is not considered in the present analysis. The overall wear depth (Δz) is assumed to be overestimated.

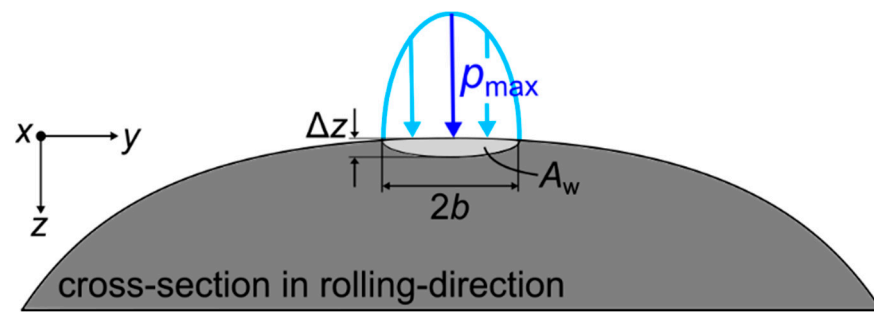


Figure 6. Relation between wear depth (Δz) calculated for the 2D cut containing (p_{\max}) through the contact patch and the wear area (A_w) in the cross section in the rolling direction.

2.1.2. Rolling Contact Fatigue (RCF) Map

The present RCF model accounts for two well-known types of fatigue in turnout components: surface-initiated fatigue and subsurface-initiated fatigue. Ekberg et al. [5] developed engineering models for both of these RCF types. This work combines these models with simplified contact models to integrate them into a RCF map. The predictive model for surface-initiated RCF builds on the shakedown map. The shakedown map indicates different material responses to contact loads in dependence of the vertical load normalized by the shear yield stress and the utilized traction coefficient. For example, surface flow (ratchetting) is predicted, which potentially leads to surface fatigue. The map presumes the following assumptions [5]:

- Hertz contact theory: all limitations of the Hertz contact (elastic material behavior, half-space assumption, etc.) apply [24];
- Full slip conditions: the shakedown map considers rolling and full slip conditions, whereas effects of partial slip conditions are neglected. However, partial slip is expected to be less severe than full slip, as suggested in [21,24];
- Creepage: although creepage may be an important variable determining fatigue life, the shakedown map does not explicitly take it into account [21].

Ekberg et al. [5] introduced the surface fatigue index (FI_{surf}) to measure the probability of crack initiation at the surface as:

$$FI_{\text{surf}} = \mu - \frac{k}{p_{\max}}, \quad (5)$$

where μ is the utilized friction or traction coefficient, p_{\max} is the maximum (Hertzian) contact pressure, and k is the shear yield stress for the work-hardened material. Owing to the severe shear deformation at the surface, this yield stress may be up to a factor of two larger than the initial yield stress [5]. For now, k is estimated from the tensile yield stress (σ_y) as $\sigma_y / \sqrt{3}$, following the von Mises hypothesis [34]. Fatigue indices greater than zero indicate potential RCF crack initiation. The magnitude of the fatigue index correlates with the probability of damage initiation. Originally, this model was developed for MBS simulations and applied to railway wheels [5,21]. It was also used for rails [24] and, recently, even for the railway crossing nose in combination with an FEA simulation considering elastic–plastic material behavior [18].

Dang Van et al. [20] developed a multiaxial high cycle fatigue criterion to study the initiation and propagation of surface RCF cracks. Several researchers, including [5,11], have applied the criterion to predict subsurface crack initiation in railway components such as wheels and crossings. Fatigue damage occurs if the following inequality is fulfilled [11]:

$$\tau_{\text{eq,DV}} = \tau_a(t) - \alpha_{\text{DV}} \times \sigma_h(t) < \tau_f, \quad (6)$$

where $\tau_{\text{eq,DV}}$ is the equivalent shear stress amplitude, τ_a is the shear stress amplitude, α_{DV} is the DV material parameter, σ_h is the hydrostatic stress and τ_f is the shear–torsion

fatigue limit. The DV material parameter is calculated from the experimentally measured tension-compression and shear–torsion fatigue limit [11].

Ekberg et al. [5] proposed an analytical approach to calculate the maximum shear stress amplitude ($\tau_{a,max}$) for pure rolling, presuming that no residual stresses are present in the material. The influence of frictional loading is included using the traction coefficient (μ). Assuming an elastic Hertz line contact, the maximum shear stress amplitude within the contact patch is calculated as [31]:

$$\tau_{a,max} = \frac{0.3 \times p_{max}}{2} \times (1 + \mu^2) \quad (7)$$

Wiedorn et al. [11] introduced the DV variable P_{DV} as a measure of subsurface RCF, which is calculated as:

$$P_{DV} = \frac{\tau_{a,max}}{\tau_f} \quad (8)$$

A P_{DV} value above 1 indicates subsurface damage initiation, whereas with values below 1, no damage is predicted. A magnitude of the DV index above 1 correlates with the number of cycles to damage initiation. Higher values indicate faster initiation. The implementation of the surface fatigue index model and simplified DV criterion into the standardized scheme requires a relation between the traction coefficient and the creepage. Carter proposed a creep force law that captures the longitudinal direction [35]. Carter approximated the system using a cylinder rolling on an infinite half-space and reported the following relations under the assumption of a Hertzian contact [35]:

$$\mu = \begin{cases} \left(-C \times c + \frac{1}{4} \times C^2 \times c \times |c| \right) \times f & \text{if } C \times |c| \leq 2 \\ -sgn(c) \times f & \text{if } C \times |c| > 2 \end{cases} \quad C = \frac{4 \times R}{f \times a} \quad (9)$$

where μ is the traction coefficient, C is the Carter creep force coefficient, c is the longitudinal creepage, f is the friction coefficient, a is the major semi-axis of the Hertzian contact ellipse and R is the rolling radius. For now, Carter's approach is applied to compute the creepage from the traction coefficient. In the future, however, more advanced creep force relations based on simulations or experiments can be implemented, such as those reported in [36].

The RCF map in Figure 7 shows four differently colored regimes: (a) no crack initiation (white), (b) surface cracks (yellow), (c) subsurface cracks (magenta) and (d) surface and subsurface cracks (salmon). The following material and contact parameters, which are taken from the literature for crossing steel Mn13 are presumed: $k = 335$ MPa, $\tau_f = 278$ MPa, $a = 10$ mm, $R = 478$ mm and $f = 0.3$ [11,13].

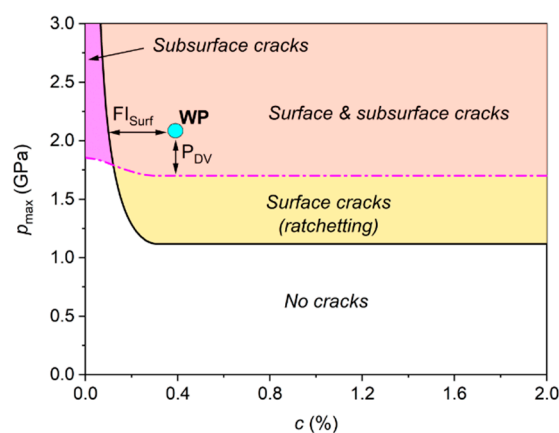


Figure 7. RCF map visualizing the limits of crack initiation at surface and subsurface locations based on local contact variables. The material and contact parameters used to calculate the RCF map are stated in the main text.

2.2. Case Study: Manganese Crossing Nose

This case study demonstrates the application of the damage assessment tool with loads transferred from a vehicle–track simulation based on FEA. A fixed manganese crossing nose from voestalpine Railway Systems GmbH (Zeltweg, Austria), which was extensively monitored in the field and investigated numerically in the past, is assessed. In particular, the wear and RCF degradation starting from a run-in state are evaluated by considering the measured crossing nose profile and different wheel types in the FEA model. The contact loads are determined in FEA postprocessing and transferred to the assessment tool. With these data, the damage indices are calculated individually from the previously introduced damage functions for each wheel type. In a further step, a simplified traffic scenario considering a series of wheel passes is generated to validate the numerical results with the field measurement data. Figure 8 outlines the workflow of the case study.

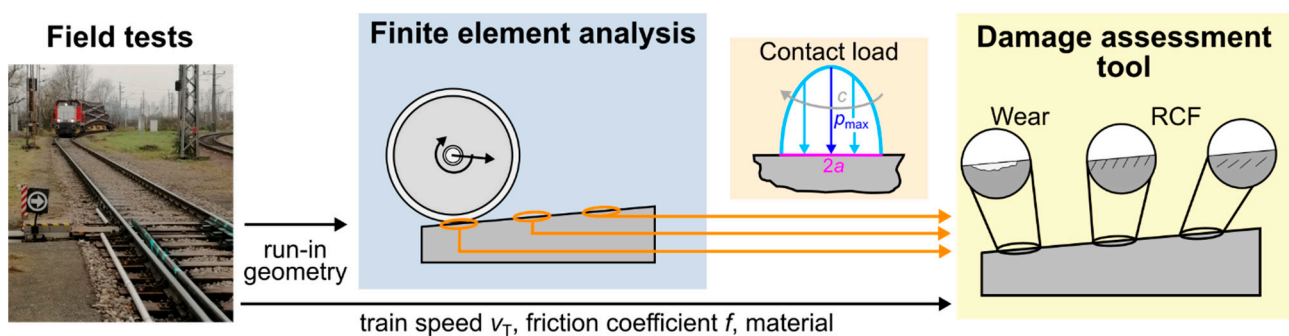


Figure 8. Workflow for the case study. Field tests provide the run-in geometry of the FEA model, the FEA computes the dynamic contact loads for different wheel profiles and the damage assessment tool predicts the damage evolution along the crossing nose.

2.2.1. Field Tests

Over a period of five years, a manganese steel crossing in Zeltweg, Austria, originating from voestalpine Railway Systems GmbH (Zeltweg, Austria) was monitored. Recently, Skrypyk et al. [13] validated their rail damage predictions based on a multidisciplinary and iterative simulation methodology using this measurement campaign. The study includes a detailed analysis of the wear and shape change of the turnout throughout the test period. The test period corresponds to accumulated traffic of approximately 65 million gross tons (MGT). The field tests included frequent rail profile measurements and a detailed photographic documentation of the surface. The monitored crossing is subject to a particularly severe load environment, as it is located in a curved turnout in a transition curve with a radius in the through route varying between 592 m and 932 m. The cant varies between 0 mm and 70 mm. Mixed traffic with a maximum vehicle speed of 90 km/h in the through route ran over the turnout. It is estimated that 90% of the traffic took the through route and 10% took the diverging route. However, the traffic distribution between facing and trailing move was not recorded. The axle loads for the passenger trains varied between 14 and 18 metric tons (for locomotives, the axle load was 22.5 metric tons). On 12 occasions over the monitoring period, the geometry of the turnout was recorded following the procedure proposed in [14]. In 16 predefined cross sections, the profile of the turnout surface was recorded using a CALIPRI non-contact measurement device (Nextsense GmbH, Graz, Austria), achieving an accuracy of $\pm 80 \mu\text{m}$. However, a potential longitudinal misalignment of the equipment by a few millimeters between repeated measurements of the same cross section is a possible source of error. After the profile measurements, the 3D crossing geometry was reconstructed (for visualization) by interpolation in between the measured 2D profiles (see Figure 9). The 16 measured cross sections correspond to the thick black lines shown along the turnout. The surface changes are calculated by referencing the measurements to the initial geometry determined immediately after installation in track. Figure 9 displays the measured geometry change of the surface after 11.9 MGT

and 19.2 MGT. The colors represent the differences between the new and the damaged profile in the direction normal to the surface. The positive direction is defined inwards. The measurement of the new profile is performed after installation in track.

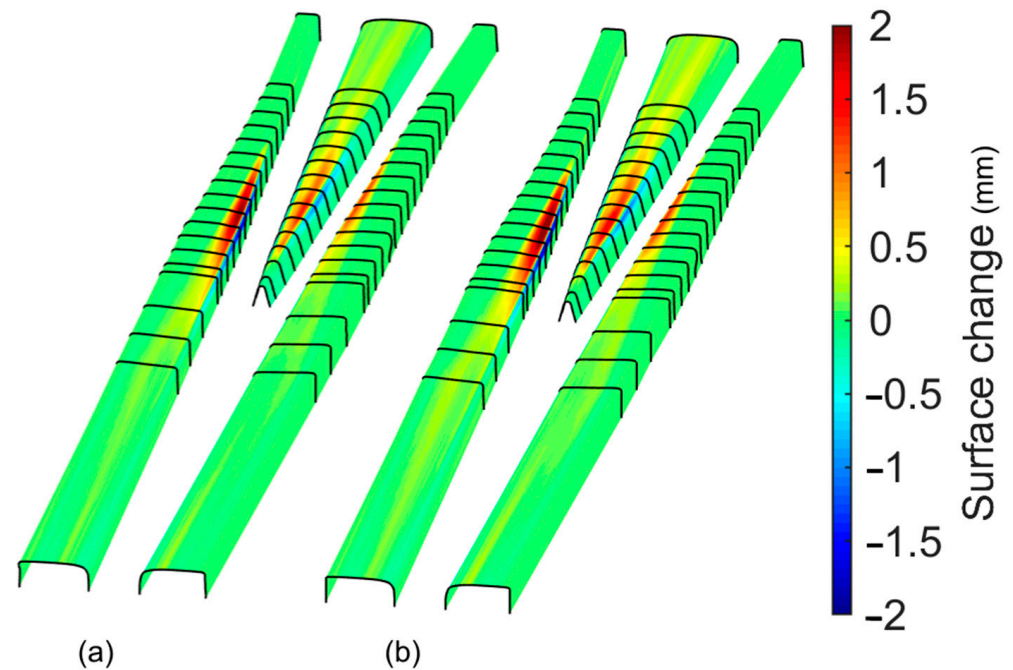


Figure 9. Measured deformation of a crossing nose after (a) 11.9 MGT and (b) 19.2 MGT of mixed traffic. The surface change corresponds to the difference between the surface geometries of the worn and new crossings.

The significant change in the rail profile occurs mainly by plastic deformation and wear during the run-in phase. A comparison between profiles measured at different times within the monitoring period allows for distinguishing between the two degradation mechanisms. The wear area (A_W) is evaluated by computing the difference between the initial area (A_0) and the current area (A) on a cross-section level [13]:

$$A_W = A_0 - A \quad (10)$$

Wiedorn et al. [11] numerically investigated the profile adaptation of a manganese crossing nose and concluded that the crossing nose adopts its geometry within the first loading cycles. Then, the plastic deformation and contact stresses stabilize. The present work uses the recorded rail profile after 11.9 MGT in the FEA to compute contact loadings representative of this run-in state. Wear and RCF crack initiation are expected to be the critical damage modes during this stage of the lifetime. The profile measurements and calculated wear areas serve as benchmarks to validate the wear model.

2.2.2. Finite Element Analysis

Wiedorn et al. developed and validated a parametrized, simplified, explicit FEA to calculate the impact of a wheel on a crossing nose with different wheel types and a measured run-in geometry [7]. In the model, the wheel moves downwards on a non-linear contact spring on the wing rail and impacts the crossing nose in the facing move. The impact of an unworn (profile ORE S1002), worn and a hollow wheel on a crossing of the EW-60E1-500-1:12 CENTRO type is studied considering the recorded run-in rail profile after 11.9 MGT traffic, as depicted in Figure 9a. Figure 10 illustrates the geometry of the three different wheel profiles.

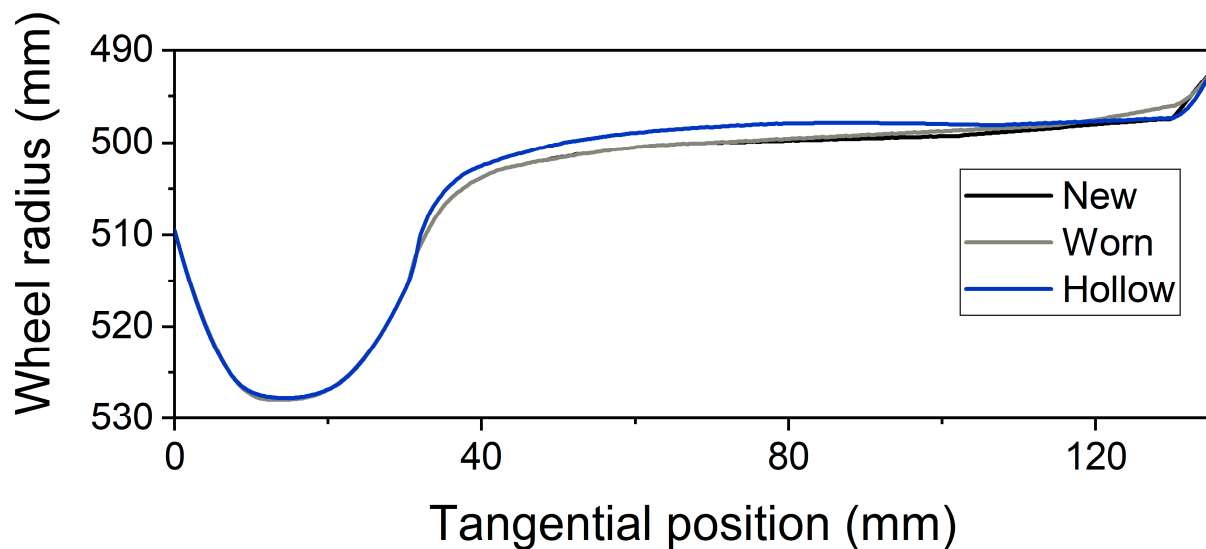


Figure 10. Unworn and worn profiles of the standard profile ORE S1002 considered in the FEA.

The mechanical system and details regarding the extraction of wheel trajectories, geometrical simplifications, the non-linear contact spring, wheel dampers and rail bedding are summarized in [1,11]. The mesh, which is built up from C3D8R elements, is refined in the contact region. Its structure is taken from [7]. In addition to the existing FEA, the slip of the wheel due to the transition from the wing rail to the crossing nose is included as proposed in [37]. In particular, the angular velocity (ω) of the wheel is increased by a slip value (s) to obtain the initial angular velocity (ω_{init}) acting at the impact:

$$\omega_{\text{init}} = \omega \times (1 + s) \quad (11)$$

For the work at hand, the slip (s) amounts to 0.83 %, 0.85 % and 0.49 % for the unworn, worn and hollow wheel profile, respectively. The differences are caused by varying impact positions and the corresponding rolling radius ratios [37]. A detailed description of the calculation procedure is given in [37].

The train velocity (v_T) is set to 90 km/h, and the static load is set to 79 kN, which are realistic loading conditions for the monitored crossing nose (see Section 2.2.1). The FEA uses a cyclic Chaboche material model with combined isotropic and kinematic hardening for the crossing nose. Table 1 summarizes the material parameters calibrated from multiaxial low cycle fatigue (LCF) material tests with as-cast Mn13. The kinematic hardening behavior is modeled by three back stresses using the parameters C_i and D_i . R_0 represents the initial yield stress, and Q and B are the parameters used to quantify the isotropic hardening. To account for the material behavior of an explosion-depth-hardened (EDH) and run-in Mn13, the initial yield stress is increased from 220 MPa (as-cast) to 580 MPa (average yield-stress EDH reported in [13]), as presented in [7]. The wheel is modeled using the linear-elastic material parameters listed in Table 1.

One impact cycle for each wheel type is computed, and the contact load variables are analyzed within postprocessing every 20 mm along the crossing nose. In total, 40 cross sections for evaluation are defined along the rail part (see Figure 11). The maximum contact pressure is determined from the Abaqus (ABAQUS CAE 2019, Dassault Systèmes, France) contact output, CPRESS, by searching for the maximum value in the cross section throughout the simulation time [38]. The contact length ($2a$) is determined from the contact time and the train speed (v_T). The creepage is calculated using the angular longitudinal velocity, as well as the rolling radius determined from the nodal coordinates in Abaqus [38].

Table 1. Material parameters used in the FEA for the wheel and crossing nose part. The hardening parameters for Mn13 are calibrated from multiaxial low cycle fatigue tests with as-cast material.

Property	Elastic (Wheel)	Mn13 (Crossing Nose)
Young's modulus (GPa)	210	201
Poisson's ratio (-)	0.3	0.3
Density (kg/m ³)	7800	7800
R_0 (MPa)	-	580
Q (MPa)	-	300
B (-)	-	10
C_1 (MPa)	-	700,000
D_1 (-)	-	4000
C_2 (MPa)	-	70,000
D_2 (-)	-	800
C_3 (MPa)	-	350
D_3 (-)	-	1

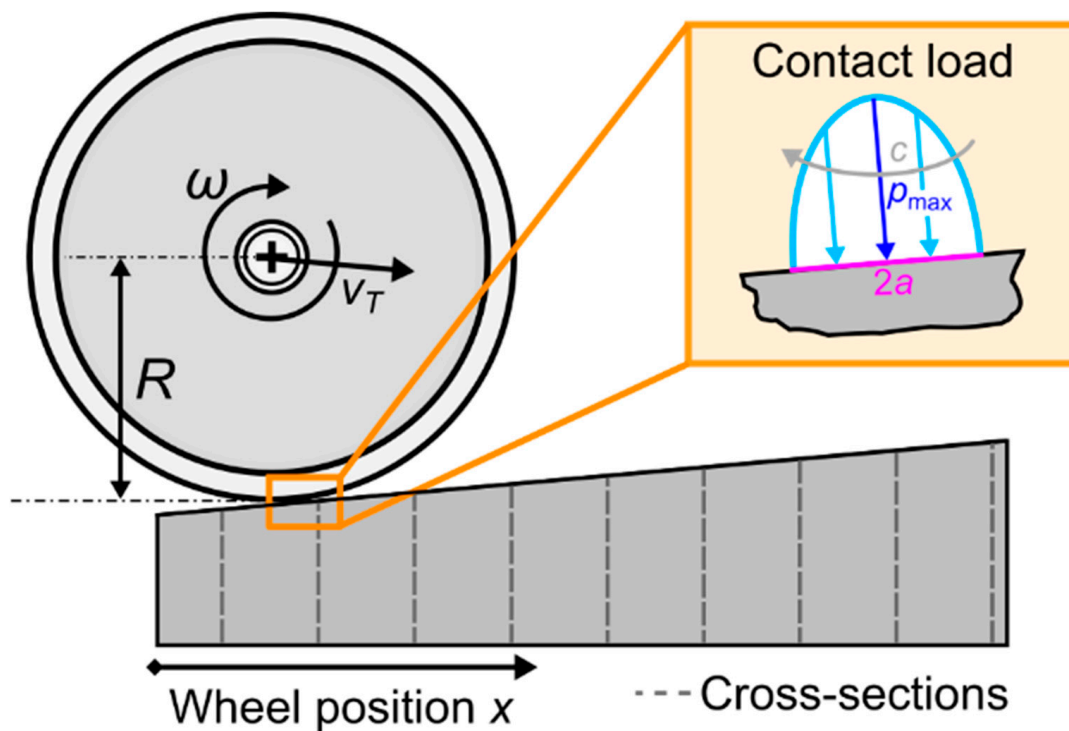


Figure 11. Definition of cross sections for local contact parameter extraction shown in a longitudinal 2D cut of the impact model.

2.2.3. Damage Assessment Tool: Material Properties

The material properties applied for the wear and RCF assessment of the run-in EDH Mn13 steel are summarized in Table 2. The local evolution of the damage along the crossing nose is assessed by transferring the contact loads from the FEA to the wear and RCF models integrated into the damage assessment tool. The predictions are verified and validated using literature data and field measurements, respectively.

Table 2. Material properties for Mn13 in the explosion-depth-hardened and run-in state required for the wear and RCF models implemented in the simplified damage assessment tool.

Damage Mechanism	Property	Magnitude	Ref.
Wear (dry contact)	Wear coefficient (K) for mild wear (-)	2.9×10^{-4}	[13]
	Hardness (H) (GPa)	3.33	[37]
RCF	Yield stress (σ_y) (MPa)	580	[13]
	Wheel rolling radius (R) (m)	0.476	[1]
	Friction coefficient (f) (dry wheel/rail friction) (-)	0.3	[1]
	Shear–torsion fatigue limit (τ_f) (MPa)	278	[1]

3. Results

In this section, the results of the case study investigating the wear and RCF damage of a manganese crossing nose are presented, together with results from the literature and field measurements. The train speed and static wheel load assumed in the FEA amount to 90 km/h and 79 kN, respectively. Figure 12 depicts the vertical contact force (F_N) computed along the run-in crossing nose for the impact of the differently worn wheels considering elastic–plastic material. Whereas for the hollow wheel, the highest F_N occurs during the first impact, for the new and worn wheel, the maximum appears during the second peak. This shift of the maximum force was previously described by Wiedorn et al. [7] for run-in crossing geometries. The effect is associated with the height change of the crossing nose due to plastic deformation and resulting “bump” formation [7]. In reality, a greater variety of wheel profiles and traffic conditions might produce a rail geometry that is not perfectly adapted to the considered wheel profiles. These geometrical mismatches between the measured rail and selected wheel profiles possibly affect the evolution of dynamic force.

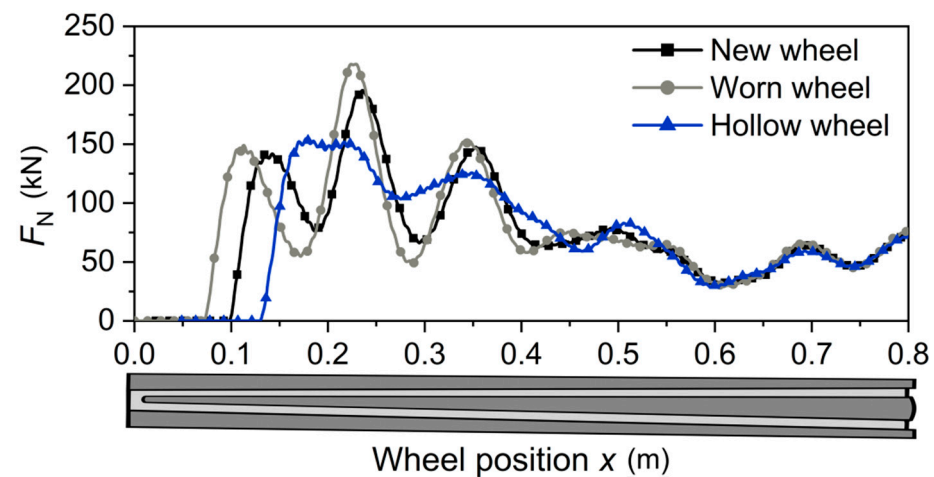


Figure 12. Vertical contact force (F_N) computed in the FEA for the impact of a new, worn and hollow wheel on the run-in crossing nose with the measured rail profile after 11.9 MGT.

3.1. Contact Loads

Figure 13 depicts the evolution of the maximum contact pressure (p_{max}), the creepage (c) and contact length ($2a$) during the impact on the crossing nose for the different wheel profiles. The parameters are extracted at the end of one loading cycle computed with elastic–plastic material behavior, as described previously.

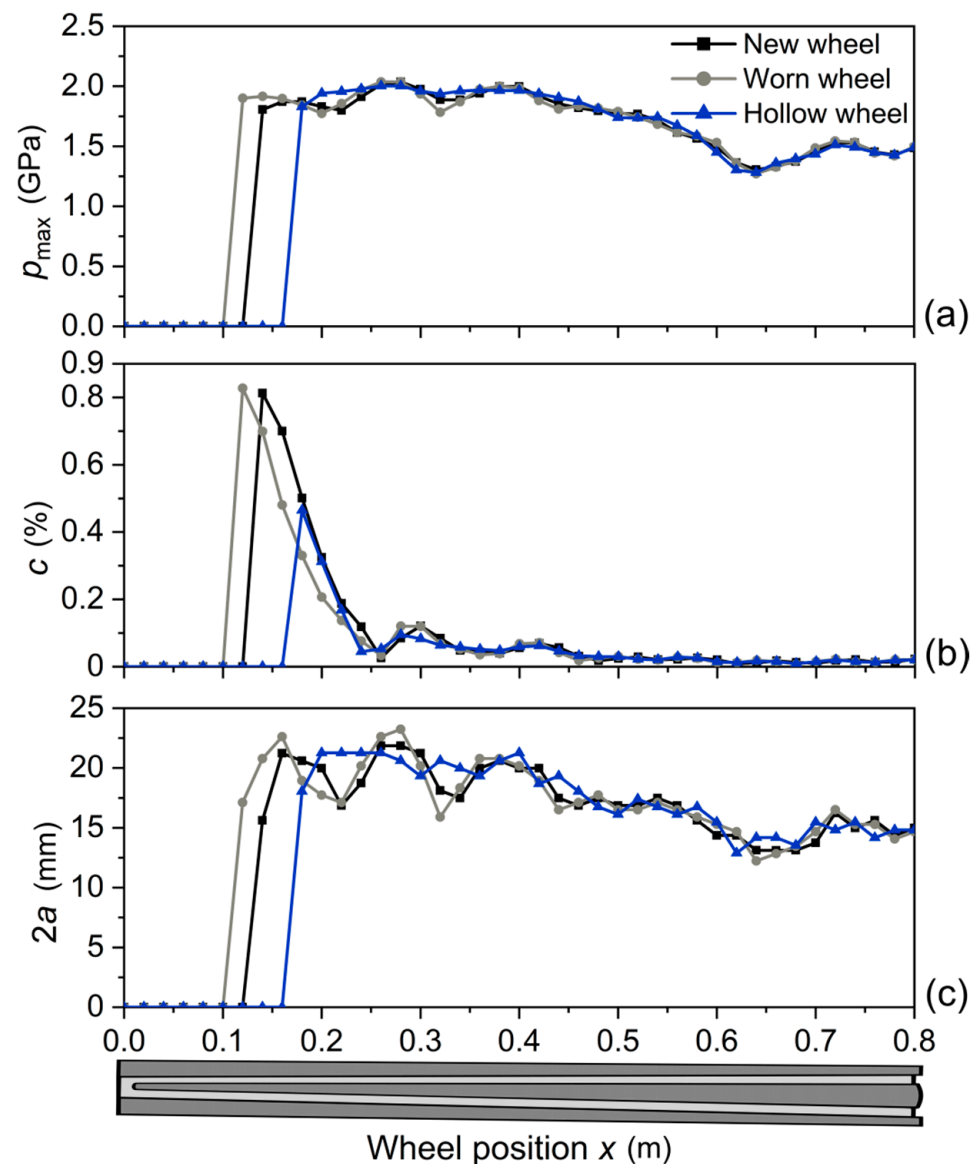


Figure 13. Loads at the local contact-patch level computed from the FEA for the impact of differently worn wheel profiles on the run-in crossing nose (11.9 MGT): (a) maximum contact pressure (p_{\max}), (b) creepage (c) and (c) contact length ($2a$).

The maxima of p_{\max} coincide with those of F_N and amount to about 2 GPa for all wheels, indicating plastic adaption within one simulation cycle. The contact length varies between 15 mm and 22 mm, with maxima coinciding with those of F_N . However, the highest creepage arises for all wheel profiles within the first impact. In this position, the relative velocity between the wheel and rail exhibits a maximum due to the transition from the wing rail. Within the first third of the crossing nose, all wheels approach the pure rolling case (c , approximately zero), as no traction is applied on the wheel.

3.2. Damage Maps

The RCF map for the explosion-depth-hardened run-in Mn13, including the different wear regimes for dry contact reported in [30], is depicted in Figure 14a. The geometrical parameters for Carter's creep force model and the required mechanical material properties are taken from Table 2. Furthermore, a constant train speed of 90 km/h is presumed. The differently colored markers in Figure 14 represent working points (WPs) corresponding to the previously computed loads at the contact-patch level of the differently worn wheels.

Whereas the sliding velocity (train speed times creepage) dictates the wear regime, the contact pressure and sliding distance (creepage times contact length) control the wear depth. Hence, an additional map is required to graphically determine the wear depth produced at a WP. The wear map in Figure 14b presents the wear depth per wheel pass as a function of the contact pressure and sliding distance valid for the mild wear regime, presuming a fixed train speed of 90 km/h.

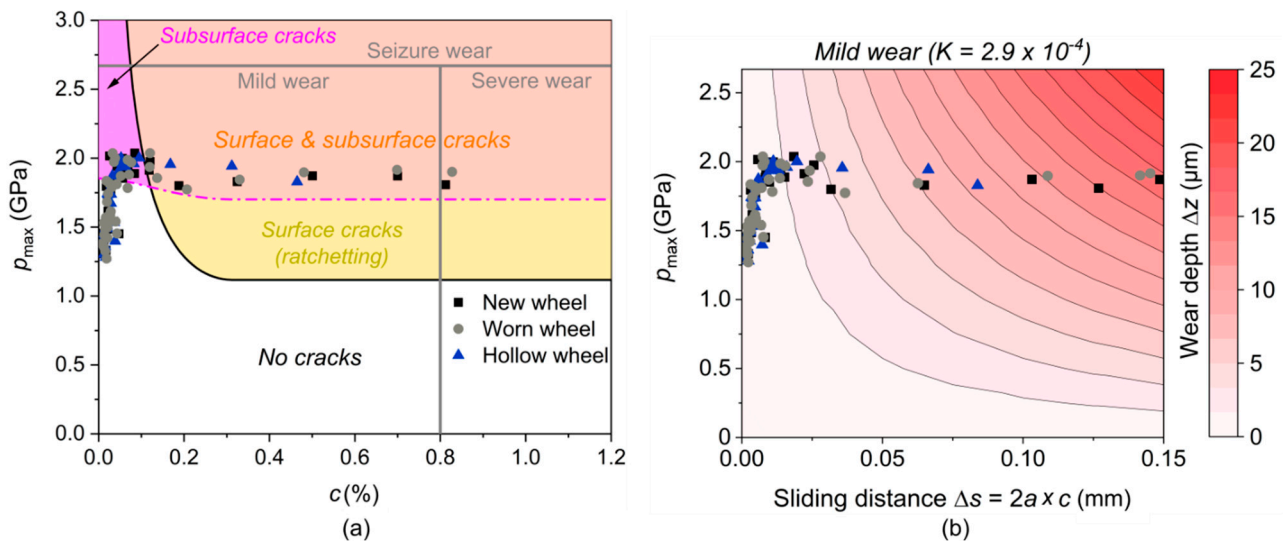


Figure 14. Wear and RCF map for Mn13 assuming the properties in Table 2 and a train speed of 90 km/h. The maps include the previously determined working points for the studied run-in crossing nose: (a) RCF map depicting crack initiation limits and wear regimes from [30] and (b) wear map for the mild wear regime with absolute wear depths per contact pass.

3.3. Evolution of Damage Indicators: Verification

In the next step, the evolution of the damage indices along the manganese crossing nose are computed from the modified wear and RCF model. To verify the present predictions, the results are plotted next to literature data in Figure 15. The maximum wear depth is predicted for all wheel profiles immediately after the first force peak. Here, the highest creepages and moderate contact pressures prevail, which are both drivers of wear. In particular, the high creepage for the new and worn wheel resulting from their impact positions accounts for the higher wear rate compared to the hollow wheel (Figure 15a). Skrypyk et al. [13] reported the evolution of the wear area rate, which correlates with Δz (see Figure 6), in different cross sections for the same crossing after 11.9 MGT mixed traffic (see Figure 15b). Note that the wear area rate and Δz depend on the contact patch size. Small contact patch sizes (i.e., tip of the crossing nose) produce high contact pressures and, consequently, high wear depths. Wider contact patches can produce high wear area rates with shallow wear depths (see Figure 6). The risk of surface crack initiation is highest at the position of the first force peak on the crossing nose. In this region, which spreads for around 150 mm, high creepage values and moderate contact pressure favor ratchetting. Afterwards, the risk of surface fatigue gradually decreases (see Figure 15c). Wei et al. [18] computed the surface fatigue index (FI_{surf}) for a comparable crossing type (54E1-1:9) and loading conditions using an FEA with elastic–plastic material behavior (see Figure 15d). The train speed, axle load and friction coefficient (dry wheel–rail friction) were set to 80 km/h, 16 t and 0.4, respectively. The material’s yield stress is 500 MPa and 700 MPa in the range of EDH Mn13 (580 MPa). The DV criterion predicts the initiation of subsurface cracks at around two-thirds of the length of the crossing nose, corresponding to regions with contact pressures higher than approximately 1.8 MPa. The maximum index exhibits a value of 1.1 and lies in the impact region (see Figure 15e). Wiedorn et al. [11] numerically computed P_{DV} along the same crossing nose type from an FEA, considering similar wheel profiles

but a new turnout geometry (see Figure 15f). A total of 55 impact cycles with 5 different wheels and an elastic–plastic material model for the as-cast Mn13 are studied. At the end, the evolution of P_{DV} is analyzed within around 300 mm after the first impact and originally plotted in a heat map. The curve shown in Figure 15f was extracted manually from this heat map. The greatest damage index amounts to 0.93, indicating no crack initiation along the crossing nose.

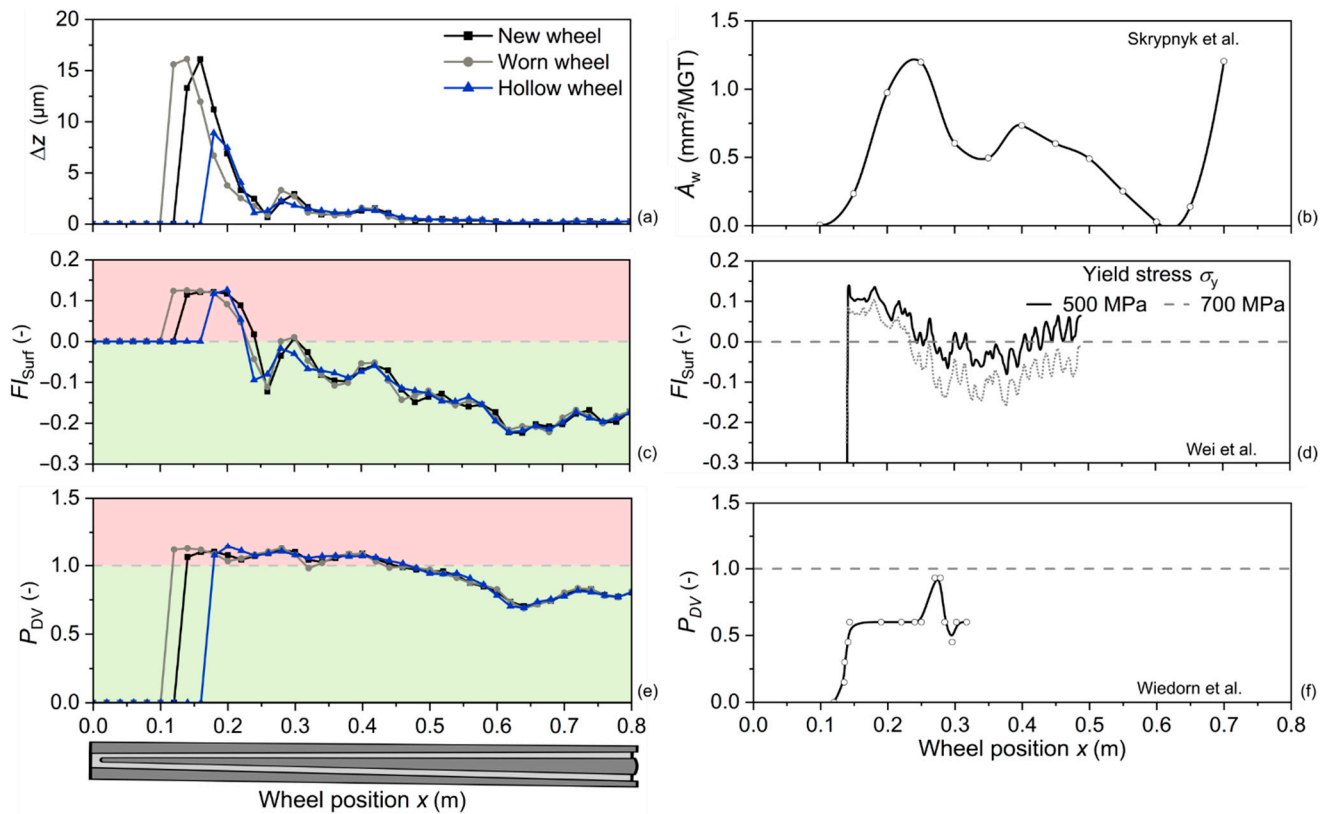


Figure 15. Local evolution of damage indices along the EDH Mn13 run-in crossing nose with measured rail profile after 11.9 MGT traffic: (a) wear depth per wheel pass (Δz), (c) surface fatigue index (F_{surf}) and (e) Dang Van index (P_{DV}). Results from comparable model evaluations in the literature: (b) wear area rate (A_w) for a manganese crossing nose considering mixed traffic conditions [13], (d) F_{surf} reported in [18] for different material yield stresses and (f) P_{DV} published in [11] for a manganese crossing nose. In (d,f), the wheel positions were adapted to coincide with present investigations, as no details were available in the publications.

3.4. Accumulated Damage: Validation

The contact-load variables transferred to the damage assessment tool capture the real contact loading in a simplified manner, and simplified wear and RCF models are applied. Therefore, the results are additionally validated with field measurement data for verification with literature data. A simplified traffic scenario that assumes an even distribution of the new, worn and hollow wheel over an accumulated load of 1 MGT is generated. Whereas the computed fatigue indices represent the maxima, the wear loss is extrapolated linearly to 1 MGT based on the outcomes for one contact patch pass. Instead of the wear depth (Δz), the wear area rate (A_w) is computed. The contact width (b) is determined by FEA postprocessing. The predictions from the RCF and wear model are opposed to a photograph and profile measurements taken within field tests, respectively (see Figure 16).

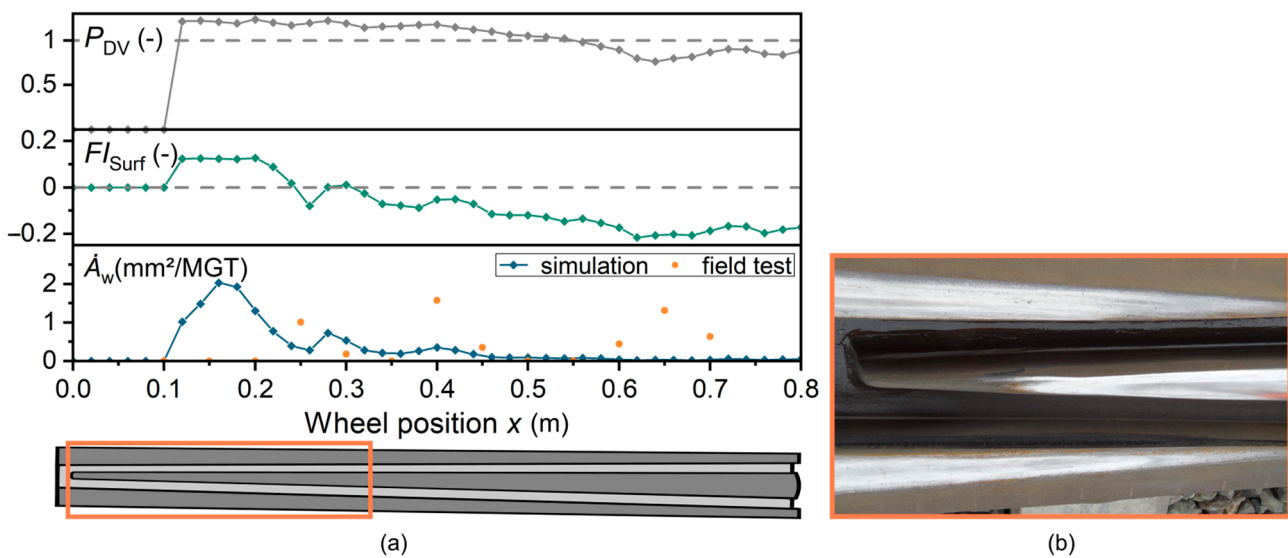


Figure 16. RCF and wear predictions for a simplified traffic scenario assuming an even distribution of the new, worn and hollow wheels over 1 MGT traffic presented in an assessment diagram: (a) local distribution of damage indices including the wear area rate (\dot{A}_w) from field measurements reported in [13] and (b) photograph of the monitored manganese crossing nose after 19.2 MGT traffic with no visible cracks at the surface provided by voestalpine Railway Systems GmbH, Leoben, Austria.

The maxima of the computed and experimental wear area (\dot{A}_w) amount to 2.03 mm²/MGT and 1.57 mm²/MGT, respectively (see Figure 16a) [13]. The fatigue indices calculated from the RCF model indicate crack initiation at and below the surface. However, in the field, no RCF is detected at the crossing nose surface after 19.2 MGT (see Figure 16b).

4. Discussion

This section evaluates the damage behavior of the investigated crossing nose based on the numerical results computed with the simplified damage assessment tool. In addition, verification with literature data and validation using field tests are discussed.

The numerical analysis used to compute the local contact loads during the impact on the crossing nose considers wheel trajectories determined based on a measured rail profile. The wheel trajectories influence the dynamic response of the different wheel profiles, resulting in differences relative to other numerical studies in the literature [11]. The hollow wheel shows the lowest variation in contact pressure and contact length (Figure 13) due to the lowest variation in the vertical force (Figure 12). Although the hollow wheel exhibits a belated impact on the crossing nose, which usually causes the highest normal impact force, the wheel trajectory and geometry of the rail profile result in a reduction in the impact and local contact force.

The working points (WPs) in the wear and RCF map in Figure 14 represent the local contact loads shown in Figure 13. Hence, their location relative to the different wear and RCF regimes indicate the overall degradation behavior. For the presently investigated crossing nose, for the majority of damaging working points (WPs), surface and subsurface RCF is likely to occur (see Figure 14a). For some WPs with low creepage values but high contact pressures, subsurface RCF will dominate. With the exception of two WPs, which lie at the boundary between the mild and severe wear regimes, all WPs fall into the mild wear regime. However, the present work attributes all WPs to the mild wear regime, assuming that the enhanced wear in the severe regime adopts the contact geometry within a few impact cycles, shifting all WPs into the mild wear regime. Consequently, from a long-term perspective, mild wear will dominate.

The local evolution of the damage indicators on the crossing nose is shown in Figure 15. The local contact loading variables, p_{max} , c and $2a$, reach their maxima next to the impact

position (see Figure 13). The three wheel types exhibit different impact positions due to differences in the wheel profile. Consequently, the dissipated energy in the contact is highest in the region of the impacts, and the damage indicators follow this trend. The comparison of the wear predictions with literature data in Figure 15a,b shows qualitative agreement. The literature reports two peaks with a similar magnitude at 250 mm and 700 mm behind the tip and a smaller peak in between. The first and second maxima qualitatively coincide with the present predictions. However, their positions and magnitudes differ. The third peak at 700 mm is missing in the present computations. In the first instance, the discrepancies are attributed to divergent wheel profiles and loading conditions (e.g., axle load and slip), as well as neglect of continuing geometrical adaptations due to wear and plastic deformation in the present framework. All these factors affect the impact position, the load on the contact-patch level and, consequently, the predicted wear loss. Additionally, the crossing head radius and contact width continuously increase from the tip, leading to increased wear loss. The predictions for surface-initiated fatigue qualitatively coincide with the literature data regarding the magnitude of FI_{surf} and its evolution. Over the first 100–150 mm after the impact, surface RCF is predicted (see Figure 15c,d). Quantitative deviations between the present predictions and literature data are attributed to varying loading conditions, as well as slightly different wheel and turnout geometries. The quantitative discrepancies of the DV indicator between the current predictions and literature data are attributed mainly to differences in the contact pressure due to differently adapted rail profiles. The literature values (see Figure 15f) were obtained from a numerical simulation, where the rail geometry perfectly adapts to the wheel profiles due to the consideration of as-cast manganese steel, which strongly plastically deforms, owing to its low initial yield strength. This run-in process reduces the contact pressures significantly to below 1.5 GPa, resulting in P_{DV} values exceeding the critical limit of 1 [11]. The run-in state measured in the field for the present FEA results from a great variety of profiles. Hence, the selected wheel profiles can be seen as extreme cases playing a minor role during the run-in phase in track. The simplifications in the RCF model, especially the neglect of residual compressive stresses, which can amount to up to 500 MPa in manganese crossing noses [11], might also lead to an overestimation of the damage index. In the end, however, the P_{DV} values predicted with the simplified assessment tool lie very close to the critical value of 1, indicating a rather low risk of crack initiation. Overall, there are discrepancies between the damaging behaviors reported in the literature for similar turnout types. However, the predictions obtained with the simplified damage assessment tool in combination with a limited number of numerical simulations are in accordance with results in the literature.

Nevertheless, a validation of the predicted degradation with recordings from field measurements is performed in the present work (see Figure 16). Whereas the magnitudes of the predicted and measured wear maxima correlate well, their positions on the crossing nose deviate. The damage assessment framework predicts the highest wear loss in the impact region. In contrast, the measured maxima are located more rearward. However, the detailed traffic conditions and corresponding wheel profile distribution leading to the measured degradation are mainly unknown. Furthermore, recording this information in the track is demanding, and the computational effort of numerical analyses generally limits the number of simulated load cases and cycles. Therefore, complex effects such as rail corrugation that might cause the observed wear behavior between 0.4 m and 0.7 m cannot be included in straightforward numerical simulations. As the detected wear rates are generally very low and in the range of the profile measuring error, the accuracy of the profile measurement is also expected to have a great influence [13]. Additionally, varying lateral wheel positions, which also impact the wear area, are disregarded in the present predictions. With respect to RCF, the predictions are not in line with surface observations in the field (Figure 16a,b). However, the computed fatigue indices lie close to their respective critical threshold values, indicating a rather low probability of crack initiation. Furthermore, the interaction between wear and RCF, which can prevent the propagation of initiated surface cracks, is not yet considered in the damage predictions. In future, detailed analyses

of the subsurface structure might be necessary to detect subsurface cracking, although such investigations are demanding and costly. In conclusion, the validation shows that the results obtained with the simplified damage assessment tool and a simple load scenario are in reasonable agreement with the field measurements. Consequently, the load transfer and modifications in damage models are proven to be in accordance with in-field experience.

5. Conclusions

The proposed implementation of the standard wear and RCF models into a simplified damage assessment tool enables a fast damage evaluation of track components. Damage computation is performed on the contact-patch level using the maximum contact pressure (p_{\max}), creepage (c) and contact length ($2a$). Visualization of material-dependent wear and RCF maps is implemented to show the damage regimes for the evaluated contact surfaces. Assessment diagrams outline the performance of the investigated track component for specific load cases.

The presented case study investigates the degradation of a run-in manganese crossing nose using load data from a finite element analysis. Its results are in agreement with the literature and in-track experience. The wear model tends to overestimate the wear area by a maximum of 30%. The main reasons for this discrepancy are attributed to neglect of the lateral wheel position, as well as the loading variation (static load and velocity) in the field. The RCF indices are in good agreement with comparable literature data and indicate a low risk of RCF crack initiation close to the impact. Observations of the simulated crossing nose in the field show no visible damage on the surface after 19.2 MGT, in accordance with the calculated low RCF risk. Further monitoring will be conducted in the field, and results of subsurface damage will be compared in future.

In conclusion, the proposed numerical tool allows track operators, as well as rail and crossing manufacturers, to predict rail and crossing damage with low computational effort. Even with simplified load cases based on a few numerical simulations, realistic predictions based on the best available damage models can be expected. Thus, the proposed tool enables a fast comparison of different materials and geometries for track components. Furthermore, the tool enables the testing of novel damage models.

Author Contributions: Conceptualization, G.S., W.D. and M.P.; methodology, G.S., W.D. and M.P.; software, G.S.; validation, G.S.; investigation, U.O.; writing—original draft preparation, G.S.; writing—review and editing, M.P., W.D., U.O., H.O., J.M. and C.B.; visualization, G.S. and M.P.; supervision, W.D.; project administration, J.M. All authors have read and agreed to the published version of the manuscript.

Funding: The authors gratefully acknowledge the financial support under the scope of the COMET program within the K2 Center “Integrated Computational Material, Process and Product Engineering (IC-MPPE)” (Project No 886385). This program is supported by the Austrian Federal Ministries for Climate Action, Environment, Energy, Mobility, Innovation and Technology (BMK) and for Digital and Economic Affairs (BMDW), represented by the Austrian Research Promotion Agency (FFG), and the federal states of Styria, Upper Austria and Tyrol.

Institutional Review Board Statement: Not applicable.

Informed Consent Statement: Not applicable.

Data Availability Statement: Not applicable.

Conflicts of Interest: The authors declare no conflict of interest.

References

1. Wiedorn, J.; Daves, W.; Ossberger, U.; Ossberger, H.; Pletz, M. Simplified explicit finite element model for the impact of a wheel on a crossing—Validation and parameter study. *Tribol. Int.* **2017**, *111*, 254–264. [[CrossRef](#)]
2. Johansson, A.; Pålsson, B.; Ekh, M.; Nielsen, J.C.O.; Ander, M.K.A.; Brouzoulis, J.; Kassa, E. Simulation of wheel–rail contact and damage in switches & crossings. *Wear* **2011**, *271*, 472–481. [[CrossRef](#)]

3. Pletz, M.; Daves, W.; Yao, W.; Ossberger, H. Rolling contact fatigue of three crossing nose materials—Multiscale FE approach. *Wear* **2014**, *314*, 69–77. [[CrossRef](#)]
4. Grossoni, I.; Hughes, P.; Bezin, Y.; Bevan, A.; Jaiswal, J. Observed failures at railway turnouts: Failure analysis, possible causes and links to current and future research. *Eng. Fail. Anal.* **2021**, *119*, 104987. [[CrossRef](#)]
5. Ekberg, A.; Kabo, E.; Andersson, H. An engineering model for prediction of rolling contact fatigue of railway wheels. *Fatigue Fract. Eng. Mater. Struct.* **2002**, *25*, 899–909. [[CrossRef](#)]
6. Magel, E.; Mutton, P.; Ekberg, A.; Kapoor, A. Rolling contact fatigue, wear and broken rail derailments. *Wear* **2016**, *366–367*, 249–257. [[CrossRef](#)]
7. Wiedorn, J.; Daves, W.; Ossberger, U.; Ossberger, H.; Pletz, M. Investigation of deformation mechanisms in manganese steel crossings using FE models. *Tribol. Int.* **2019**, *138*, 424–434. [[CrossRef](#)]
8. Wiest, M.; Daves, W.; Fischer, F.D.; Ossberger, H. Deformation and damage of a crossing nose due to wheel passages. *Wear* **2008**, *265*, 1431–1438. [[CrossRef](#)]
9. Pletz, M.; Daves, W.; Yao, W.; Kubin, W.; Scheriau, S. Multi-scale finite element modeling to describe rolling contact fatigue in a wheel–rail test rig. *Tribol. Int.* **2014**, *80*, 147–155. [[CrossRef](#)]
10. Pletz, M.; Daves, W.; Ossberger, H. A wheel set/crossing model regarding impact, sliding and deformation—Explicit finite element approach. *Wear* **2012**, *294–295*, 446–456. [[CrossRef](#)]
11. Wiedorn, J.; Daves, W.; Ossberger, U.; Ossberger, H.; Pletz, M. Numerical assessment of materials used in railway crossings by predicting damage initiation—Validation and application. *Wear* **2018**, *414–415*, 136–150. [[CrossRef](#)]
12. Kassa, E.; Andersson, C.; Nielsen, J.C.O. Simulation of dynamic interaction between train and railway turnout. *Veh. Syst. Dyn.* **2006**, *44*, 247–258. [[CrossRef](#)]
13. Skrypnik, R.; Ossberger, U.; Pålsson, B.A.; Ekh, M.; Nielsen, J.C.O. Long-term rail profile damage in a railway crossing: Field measurements and numerical simulations. *Wear* **2021**, *472–473*, 203331. [[CrossRef](#)]
14. Ossberger, U.; Kollment, W.; Eck, S. Insights towards Condition Monitoring of Fixed Railway Crossings. *Procedia Struct. Integr.* **2017**, *4*, 106–114. [[CrossRef](#)]
15. Archard, J.F. Contact and Rubbing of Flat Surfaces. *J. Appl. Phys.* **1953**, *24*, 981–988. [[CrossRef](#)]
16. Pombo, J.; Ambrósio, J.; Pereira, M.; Lewis, R.; Dwyer-Joyce, R.; Ariaudo, C.; Kuka, N. Development of a wear prediction tool for steel railway wheels using three alternative wear functions. *Wear* **2011**, *271*, 238–245. [[CrossRef](#)]
17. Lewis, R.; Magel, E.; Wang, W.; Olofsson, U.; Lewis, S.; Slatter, T.; Beagles, A. Towards a standard approach for the wear testing of wheel and rail materials. *Proc. Inst. Mech. Eng. F J. Rail Rapid Transit* **2017**, *231*, 760–774. [[CrossRef](#)]
18. Wei, Z.; Núñez, A.; Liu, X.; Dollevoet, R.; Li, Z. Multi-criteria evaluation of wheel/rail degradation at railway crossings. *Tribol. Int.* **2020**, *144*, 106107. [[CrossRef](#)]
19. Daves, W.; Krácalík, M.; Scheriau, S. Analysis of crack growth under rolling-sliding contact. *Int. J. Fatigue* **2019**, *121*, 63–72. [[CrossRef](#)]
20. Van, K.; Griveau, B. On a new multiaxial fatigue limit criterion—Theory and Application. In *Biaxial and Multiaxial Fatigue, EGF 3*; Mechanical Engineering Publications, Ltd.: London, UK, 1989; pp. 479–496.
21. Dirks, B.; Enblom, R. Prediction model for wheel profile wear and rolling contact fatigue. *Wear* **2011**, *271*, 210–217. [[CrossRef](#)]
22. Mazzù, A.; Petrogalli, C.; Faccoli, M. An integrated model for competitive damage mechanisms assessment in railway wheel steels. *Wear* **2015**, *322–323*, 181–191. [[CrossRef](#)]
23. Karttunen, K.; Kabo, E.; Ekberg, A. Estimation of gauge corner and flange root degradation from rail, wheel and track geometries. *Wear* **2016**, *366–367*, 294–302. [[CrossRef](#)]
24. Boyacioglu, P.; Bevan, A. Prediction of rail damage using a combination of Shakedown Map and wheel-rail contact energy. *Wear* **2020**, *460–461*, 203457. [[CrossRef](#)]
25. Nielsen, J.C.O.; Pålsson, B.A.; Torstensson, P.T. Switch panel design based on simulation of accumulated rail damage in a railway turnout. *Wear* **2016**, *366–367*, 241–248. [[CrossRef](#)]
26. Ma, X.; Wang, P.; Xu, J.; Chen, R.; Wang, J. Assessment of non-Hertzian wheel-rail contact models for numerical simulation of rail damages in switch panel of railway turnout. *Wear* **2019**, *432–433*, 102912. [[CrossRef](#)]
27. Zani, N.; Ekh, M.; Ekberg, A.; Mazzù, A. Application of a semianalytical strain assessment and multiaxial fatigue analysis to compare rolling contact fatigue in twin-disk and full-scale wheel/rail contact conditions. *Fatigue Fract. Eng. Mater. Struct.* **2021**, *37*, 478. [[CrossRef](#)]
28. Meyer, K.A.; Skrypnik, R.; Pletz, M. Efficient 3d finite element modeling of cyclic elasto-plastic rolling contact. *Tribol. Int.* **2021**, *161*, 107053. [[CrossRef](#)]
29. Daves, W.; Kubin, W.; Scheriau, S.; Pletz, M. A finite element model to simulate the physical mechanisms of wear and crack initiation in wheel/rail contact. *Wear* **2016**, *366–367*, 78–83. [[CrossRef](#)]
30. Jendel, T. Prediction of wheel profile wear—Comparisons with field measurements. *Wear* **2002**, *253*, 89–99. [[CrossRef](#)]
31. Johnson, K.L. *Contact Mechanics*; Cambridge University Press: Cambridge, UK; New York, NY, USA; Port Melbourne, Australia; Madrid, Spain; Cape Town, South Africa, 1985, ISBN 0521255767.
32. Cremona, M.A.; Liu, B.; Hu, Y.; Bruni, S.; Lewis, R. Predicting railway wheel wear under uncertainty of wear coefficient, using universal kriging. *Reliab. Eng. Syst.* **2016**, *154*, 49–59. [[CrossRef](#)]

33. Schelle, H. Radverschleissreduzierung für Eine Güterzuglokomotive Durch Optimierte Spurführung. Ph.D. Thesis, Technische Universität Berlin, Berlin/Heidelberg, Germany, 2014.
34. Besson, J.; Cailletaud, G.; Chaboche, J.-L.; Forest, S. *Non-Linear Mechanics of Materials*; Springer Science+Business Media B.V: Dordrecht, The Netherlands, 2010, ISBN 978-90-481-3355-0.
35. Enblom, R. Deterioration mechanisms in the wheel–rail interface with focus on wear prediction: A literature review. *Veh. Syst. Dyn.* **2009**, *47*, 661–700. [[CrossRef](#)]
36. Vollebregt, E.; Six, K.; Polach, O. Challenges and progress in the understanding and modelling of the wheel–rail creep forces. *Veh. Syst. Dyn.* **2021**, *59*, 1026–1068. [[CrossRef](#)]
37. Wiedorn, J.; Daves, W.; Ossberger, U.; Ossberger, H.; Pletz, M. Finite element model for predicting the initiation of subsurface damage in railway crossings—A parametric study. *Proc. Inst. Mech. Eng. F J. Rail Rapid Transit* **2019**, *233*, 614–628. [[CrossRef](#)]
38. Dassault Systèmes. *Abaqus 2019 User Manual*; Dassault Systèmes: Vélizy-Villacoublay, France, 2019.